Nonlinear theory of short-wavelength free-electron lasers

H. P. Freund
Science Applications International Corporation, McLean, Virginia 22102
(Received 11 May 1995)

The nonlinear evolution of free-electron laser (FEL) amplifiers is studied for infrared and shorter wavelengths. The configuration of interest consists in the propagation of an energetic electron beam through a drift tube in the presence of a periodic wiggler magnetic field with planar symmetry. A three-dimensional formulation is derived in which the electromagnetic field is represented as an expansion of Gaussian optical modes. Since the wiggler model is characterized by planar symmetry, the Gauss-Hermite modes are used for this purpose. A set of nonlinear differential equations is derived for the evolution of the amplitude and phase of each mode, and they are solved simultaneously in conjunction with the three-dimensional Lorentz force equations for an ensemble of electrons in the presence of the magneto-static wiggler, self-electric and self-magnetic fields due to the charge and current distributions of the beam, and the electromagnetic fields. It is important to note that no wiggler average is used in the integration of the electron trajectories. This permits the self-consistent modeling of effects associated with (1) the injection of the beam into the wiggler, (2) emittance growth due to inhomogeneities in the wiggler and radiation fields as well as due to the self-fields, (3) the effect of wiggler imperfections, and (4) betatron oscillations. The optical guiding of the radiation field is implicitly included in the formulation. This approach has important practical advantages in analyzing FELs, since it is necessary only to characterize the beam upon injection into the wiggler, and the subsequent evolution is treated self-consistently. Numerical simulations are performed for two examples corresponding to an infrared FEL at wavelengths near 3.5 μm, and an x-ray FEL operating in the neighborhood of 1.4 Å wavelengths corresponding to the proposed linear coherent light source (LCLS) at the Stanford Linear Accelerator Center. Results for both cases indicate that the more severe limiting factor on the performance of the FEL is the beam emittance. For the infrared example, the transition to the thermal regime occurs for an axial energy spread of $\Delta\gamma_z/\gamma_0 \approx 0.19\%$, and optimal performance is obtained for $\Delta\gamma_z/\gamma_0 < 0.1\%$ and γ is the relativistic factor. This restriction is more severe for the LCLS parameters, for which the thermal transition is found for $\Delta\gamma_z/\gamma_0 \approx 0.05\%$ and optimal performance requires $\Delta\gamma_z/\gamma_0 \leq 0.01\%$. Wiggler imperfections are found to be a much less important constraint on FEL design. Simulations indicate that there is no coherent "walkoff" of the beam from the symmetry axis due to wiggler imperfections, and that the radiation field is sufficiently guided by the interaction that no severe degradation is found in the extraction efficiency or growth rate for moderate levels of wiggler fluctuations.

PACS number(s): 41.60.Cr, 41.60.−m, 41.50.+h, 52.75.Ms

I. INTRODUCTION

The free-electron laser (FEL) has been demonstrated to operate at spectral ranges from the microwave through the ultraviolet [1–16] using a wide variety of accelerators, including modulators, pulse line accelerators, electrostatic accelerators, induction and rf linacs, and storage rings. The fundamental physics of the interaction relies upon stimulated scattering due to the ponderomotive potential created of the beating of a periodic magnetostatic wiggler and the radiation field in the presence of an energetic electron beam [17]. Wiggler magnets have been built with helical, planar, and azimuthal symmetry and FELs have been configured as master oscillator power amplifiers (MOPAs), oscillators, and super-radiant amplifiers. The term *super-radiant amplifier* was originally used to denote a device in which the radiation grows from noise in a single pass through the wiggler; however, the term self-amplified spontaneous emission (SASE) has recently become more widely used for this class of device.

MOPAs and SASE devices have typically been employed longer (millimeter and submillimeter) wavelengths using high-current but relatively low-energy electron beams. In this parameter regime, the FEL grain is sufficiently high to drive the signal to saturation in a single pass. In contrast, short-wavelength FELs (defined herein as near-infrared wavelengths and below) have required higher-energy beams. Since the currents available from most accelerators capable of producing the necessary energies were not high enough to yield single-pass gains suitable for amplifier operation, these FELs have typically been configured as oscillators. However, recently rf linac designs have been proposed in which the peak currents are high enough to make amplifier operation possible. The purpose of this paper is to address a range of important issues relevant to short-wavelength FEL amplifiers.

In this paper, a three-dimensional nonlinear formulation of the interaction in short-wavelength FELs is described and applied to the study of several devices of current interest in the infrared and x-ray spectra. The technique employed is similar to a formulation developed

previously [18–20] that was applied to long-waveguide FELs. The fundamental technique is based upon a representation of the electromagnetic field as a superposition of vacuum modes. The long-wavelength formulation was tailored to treat the modes in both cylindrical and rectangular waveguides. For the present case of short-wavelength FELs, Gaussian optical modes will be used. Nonlinear equations governing the evolution of the amplitude and phase of each mode are derived by taking an average of Maxwell's equations over the wave period. This eliminates the fast time- and space-scale variation from the equations, which greatly reduces the computational requirements. These equations are integrated simultaneously with the three-dimensional Lorentz force equations for an ensemble of electrons subject to the total aggregate of static and fluctuating fields. This includes the magnetostatic wiggler, the electromagnetic radiation fields, and the static self-electric and self-magnetic fields produced by the bulk charge and current densities of the beam [21]. However, collective Raman effects associated with the fluctuating fields of the beam space-charge waves are neglected in the analysis because the frequencies of interest are much higher than the beam plasma frequency.

It is important to emphasize that no average is performed over the Lorentz force equations. This permits the simulation of the entire wealth of three-dimensional phenomena in the FEL including, but not limited to, emittance growth in the injection of the beam into the wiggler and during the course of the interaction, the effect of transverse inhomogeneities in the fields which manifests as an effective energy spread leading to resonance broadening and betatron oscillations, optical guiding of the radiation field by the beam, and the self-consistent modeling of wiggler imperfections.

Two wiggler models are used, both of which have planar symmetry. The reason for this is that most of the short-wavelength FELs, as well as the undulators used in synchrotron light sources, are planar designs. In view of this wiggler symmetry, the preferred choice for the optical modes are the Gauss-Hermite modes. It should be observed in this regard that the drift tube in which the electron beam propagates also constitutes a waveguide, and that Gaussian modes do not rigorously satisfy the boundary condition on the drift tube wall. As a result, it is implicitly assumed that the spot size of the Gaussian radiation beam is much less than the radius of the drift tube. Furthermore, since the radiation is guided by the beam, it is also assumed that the beam radius is much smaller than the drift tube radius.

The organization of the paper is as follows. The general mathematical formulation is described in Sec. II. This includes the wiggler geometry, the Gauss-Hermite modes, the dynamical equations for the amplitudes and phases of the Gaussian modes, and the electron dynamics. Two numerical examples are discussed in Sec. III. The first is an infrared FEL operating at a wavelength of about 3.5 μm. The second is relevant to an x-ray FEL design which is under consideration at the Stanford Linear Accelerator Center (SLAC) [22] which is referred to as the Linear Coherent Light Source (LCLS) utilizing the SLAC linac. This is a 15-GeV design which is intended to operate at wavelengths ranging from 1 to 4 Å. In both cases, issues relating to the extraction efficiency, the sensitivity to beam emittance, the mode spectrum, and the effect of wiggler imperfection are examined. A summary and discussion is given in Sec. IV.

II. MATHEMATICAL FORMULATION

The physical configuration of interest is one in which an energetic electron beam propagates through a circular drift tube in the presence of a planar wiggler magnetic field. Since we are interested in radiation in the infrared spectrum and still shorter wavelengths, the electromagnetic field is expressed in terms of Gaussian optical modes. Furthermore, because the wiggler has a planar symmetry, it is most convenient to employ a superposition of Gauss-Hermite modes. The electron dynamics are treated using the full three-dimensional Lorentz force equations with these magnetostatic and electromagnetic fields. In addition, collective effects arising from the bulk self-electric and self-magnetic fields due to the charge and current distribution of the beam are included as well under the assumption of a circular pencil beam geometry. However, since the wavelength of interest is less than or of the order of several micrometers, the collective Raman effects due to the beam space-charge waves are neglected.

A. Wiggler geometry

Two different models of the wiggler field are used. One model is based upon a planar wiggler generated by a magnet stack with parabolically shaped pole faces [1], and has the form

$$\mathbf{B}_w(\mathbf{x})=B_w(z)\left\{\cos k_w z\left[\hat{\mathbf{e}}_x \sinh\left[\frac{k_w x}{\sqrt{2}}\right]\sinh\left[\frac{k_w y}{\sqrt{2}}\right]+\hat{\mathbf{e}}_y \cosh\left[\frac{k_w x}{\sqrt{2}}\right]\cosh\left[\frac{k_w y}{\sqrt{2}}\right]\right]\right.$$
$$\left.-\sqrt{2}\hat{\mathbf{e}}_z \sin k_w z \cosh\left[\frac{k_w x}{\sqrt{2}}\right]\sinh\left[\frac{k_w y}{\sqrt{2}}\right]\right\}, \quad (1)$$

where B_w denotes the wiggler amplitude and $k_w \equiv 2\pi/\lambda_w$ denotes the wiggler wave number corresponding to the wiggler period λ_w. This type of wiggler provides enhanced focusing of the electron beam in the plane transverse to the direction of bulk electron flow. The other wiggler model is one in which focusing in the direction of the wiggler-induced transverse oscillation is described by a polynomial increase in wiggler amplitude.

This is the x direction for the present choice of wiggler geometry, and the components of the field are represented as

$$B_{w,x}(\mathbf{x})=\left[\left[\sin k_w z-\frac{\cos k_w z}{k_w}\frac{d}{dz}\right]B_w(z)\right]\times\left[\sinh k_w y-\frac{Y(k_w y)}{2k_w^2}\frac{d^2}{dx^2}\right]\frac{1}{k_w}\frac{d}{dx}X(x)\ , \tag{2}$$

$$B_{w,y}(\mathbf{x})=\left[\left[\sin k_w z-\frac{\cos k_w z}{k_w}\frac{d}{dz}\right]B_w(z)\right]\times\left[\cosh k_w y-\frac{k_w y\sinh k_w y}{2k_w^2}\frac{d^2}{dx^2}\right]X(x)\ , \tag{3}$$

$$B_{w,z}(\mathbf{x})=B_w(z)\cos k_w z\left[\sinh k_w y-\frac{Y(k_w y)}{k_w^2}\times\left[1+\frac{1}{k_w^2}\frac{d^2}{dx^2}\right]\frac{d^2}{dx^2}\right]X(x)\ , \tag{4}$$

where $Y(k_w y)\equiv k_w y\cosh k_w y-\sinh k_w y$, and

$$X(x)\equiv 1+\frac{1}{2}\left[\frac{x}{\alpha_x}\right]^{2m} \tag{5}$$

describes the enhanced focusing in terms of two free parameters: the order of the polynomial m and the scale length α_x. Observe that in the limit in which the wiggler amplitude is constant and $X(x)\to 1$ (i.e., when $\alpha_x\to\infty$), then this wiggler reduces to the well-known three-dimensional form of a flat pole face wiggler $\mathbf{B}_w(\mathbf{x})\to B_w[\hat{\mathbf{e}}_y\sin k_w z\cosh k_w y+\hat{\mathbf{e}}_z\cos k_w z\sinh k_w y]$.

The wiggler amplitudes in each case are permitted to vary with axial position in order to model such effects as (1) the adiabatic injection of the beam into the wiggler, (2) efficiency enhancement using a tapered wiggler amplitude, and (3) the inclusion of imperfections in the wiggler. As such, we can write the amplitude as a superposition of systematic and random components

$$B_w(z)=B_w^{(s)}(z)+\Delta B_w(z)\ , \tag{6}$$

where the systematic $B_w^{(s)}$ describes the adiabatic entry taper as well as the uniform amplitude and systematic taper for efficiency enhancement, and the random component ΔB_w can either be chosen using a random number generator or the measured imperfections from an actual wiggler magnet.

We choose a systematic amplitude variation of the form

$$B_w^{(s)}(z)=\begin{cases}B_w\sin^2\left[\dfrac{k_w z}{4N_w}\right], & 0\le z\le N_w\lambda_w\\ B_w, & N_w\lambda_w<z\le z_0\\ B_w[1+k_w\varepsilon_w(z-z_0)], & z_0<z\ ,\end{cases} \tag{7}$$

where B_w denotes the uniform wiggler amplitude, N_w is the length of the adiabatic entry taper in wiggler periods, z_0 is the start of the downstream amplitude taper for efficiency enhancement, and ε_w represents the slope of the taper.

The random component of the amplitude is determined by specifying the magnitude of the amplitude variations at periodic intervals of a wiggler period $\Delta z=\lambda_w/N_p$, and then mapping the amplitude between these points in a continuous fashion. Thus we choose a sequence of wiggler imperfections, $\Delta B_n=\Delta B_w(n\Delta z)$ either from a random number generator or from the measured variations in a specific wiggler magnet. The only restriction placed on this sequence is that $\Delta B_w=0$ over the entry taper region in order to ensure a positive definite amplitude. The variation in $\Delta B_w(z)$ between these points [i.e., $n\Delta z\le z\le(n+1)\Delta z$] is given by

$$\Delta B_w(n\Delta z+\delta z)=\Delta B_n+[\Delta B_{n+1}-\Delta B_n]\sin^2\left[\frac{\pi}{2}\frac{\delta z}{\Delta z}\right]\ , \tag{8}$$

where $0\le\delta z\le\Delta z$. This method for the treatment of wiggler imperfections has been previously applied to long-wavelength FELs in which the electromagnetic fields are confined in a waveguide [23,24].

Free-electron lasers have been constructed using both wiggler types. The first design using parabolic pole faces was constructed by Phillips [1], and the second wiggler type has been used in a harmonic FEL experiment at the Naval Research Laboratory [25]. Both field types provide enhanced focusing which is necessary for the propagation of intense beams. It is important to note, however, that while the parabolic pole face model in Eq. (1) is curl- and divergence-free in the case of a uniform amplitude, the curl and divergence do not vanish identically when the amplitude is allowed to vary in z. This simply means that the fringing fields associated with variations in the amplitude are not included in the model. Since it is important to ensure that the wiggler model be self-consistent in order for the theory to be valid, and since the curl and divergence are proportional to the slope of the amplitude, we must restrict the use of this model to cases where the amplitude changes slowly with axial position. In contrast, both the divergence and the z component of the curl of the second wiggler model can be shown to be divergence-free for any smooth variation in the amplitude. In addition, while the transverse components of the curl do not vanish identically, they are small for most cases of interest.

B. Electromagnetic fields

The electromagnetic fields are represented in terms of the Gauss-Hermite optical modes. This constitutes a complete basis set which is consistent with the planar symmetry imposed by the wiggler geometry. It should be noted, however, that Gaussian optical modes must be

used with some caution because the drift tube in which the electron beam propagates also constitutes a waveguide, and the Gaussian modes do not rigorously satisfy the boundary conditions on the drift tube wall. As a result, the analysis must be restricted to cases where the radiation spot size is much smaller than the radius of the drift tube. Since the radiation will be guided by the interaction with the electron beam, this condition is equivalent to the requirement that the electron beam radius be much less than the drift tube radius.

The vector potential of the Gauss-Hermite modes can be expressed as [26]

$$\delta\mathbf{A}(\mathbf{x},t)=\sum_{l,n=0}^{\infty}\delta A_{l,n}(z)\frac{w_0}{w}\exp(-r^2/w^2)H_n\left[\frac{\sqrt{2}y}{w}\right]\times\left\{H_l\left[\frac{\sqrt{2}x}{w}\right]\hat{\mathbf{e}}_x\sin\varphi_{l,n}-\frac{\sqrt{2}}{k_{l,n}w}\hat{\mathbf{e}}_z\left[\frac{\sqrt{2}x}{w}\frac{z}{z_0}H_l\left[\frac{\sqrt{2}x}{w}\right]\sin\varphi_{l,n}+\left[\frac{\sqrt{2}x}{w}H_l\left[\frac{\sqrt{2}x}{w}\right]-H_l'\left[\frac{\sqrt{2}x}{w}\right]\right]\cos\varphi_{l,n}\right]\right\}, \tag{9}$$

where H_n denotes the Hermite polynomials, w_0 denotes the spot size at the radiation waist, and for frequency and wave number $(\omega,k_{l,n})$ the phase is given by

$$\varphi_{l,n}=\int_0^z dz'k_{l,n}(z')+\frac{k_0 r}{2R}-(l+n+1)\tan^{-1}\left[\frac{z}{z_0}\right]-\omega t\ . \tag{10}$$

In addition, $k_0\equiv\omega/c$ is the free-space wavelength, $w^2\equiv w_0^2(1+z^2/z_0^2)$, $R(z)\equiv z(1+z_0^2/z^2)$, and $z_0\equiv k_0w_0^2/2$ is the Rayleigh length. Observe that the amplitude and wave number of each mode is allowed to vary slowly in z to describe the growth of the wave as well as the dielectric effect of the beam on the dispersion. The Poynting flux for each mode can be written as

$$P_{l,n}=\frac{2^{l+n}l!n!}{16}\omega k_{l,n}w_0^2\delta A_{l,n}^2\ . \tag{11}$$

It should be remarked that this representation is correct to first order in $(k_{l,n}w)^{-1}\approx\lambda/w$, where λ denotes the wavelength; hence, this representation is valid only as long as the spot size is much greater than the wavelength. Observe as well that these modes approximate TEM modes only as long as $\lambda\ll w$. For all cases of interest in this paper, this inequality is satisfied, and it will prove convenient to use the TEM approximation for the field.

C. Dynamical equations

The dynamical equations which govern the evolution of the amplitude and wave number of each mode are found by substitution of the mode representation (9) into Maxwell's equations after averaging the equations over a wave period and orthogonalization in the transverse mode structure. The procedure is formally equivalent to that described for long-wavelength FELs [18–20], and results in equations of the form

$$\left[\frac{d^2}{dz^2}+\left[\frac{\omega^2}{c^2}-k_{l,n}^2\right]\right]\delta a_{l,n}=\frac{4\omega_b^2}{c^2}\frac{1}{2^{l+n}l!n!}\frac{w_0}{w}\left\langle\frac{v_x}{|v_z|}\exp(-r^2/w^2)H_l\left[\frac{\sqrt{2}x}{w}\right]H_n\left[\frac{\sqrt{2}y}{w}\right]\sin\varphi_{l,n}\right\rangle, \tag{12}$$

and

$$2k_{l,n}^{1/2}\frac{d}{dz}(k_{l,n}^{1/2}\delta a_{l,n})=\frac{4\omega_b^2}{c^2}\frac{1}{2^{l+n}l!n!}\frac{w_0}{w}\left\langle\frac{v_x}{|v_z|}\exp(-r^2/w^2)H_l\left[\frac{\sqrt{2}x}{w}\right]H_n\left[\frac{\sqrt{2}y}{w}\right]\cos\varphi_{l,n}\right\rangle, \tag{13}$$

where $\delta a_{l,n}\equiv e\delta A_{l,n}/m_ec^2$, ω_b is the beam plasma frequency, $\mathbf{v}$ is the instantaneous electron velocity, e and m_e are the electronic charge and rest mass, and c is the speed of light *in vacuo*.

The averaging operator in Eqs. (12) and (13) is defined over an ensemble of electrons injected into the wiggler within one wave period. The initial momentum space distribution is chosen to be monoenergetic but with a pitch-angle spread. This can be thought of as having a zero energy spread but a nonzero emittance. The specific form of the distribution is

$$F_0(\mathbf{p}_0)=A\exp[-(p_{z0}-p_0)^2/\Delta p_z^2]\times\delta[p_0^2-p_{10}^2-p_{z0}^2]H(p_{z0})\ , \tag{14}$$

where the subscript 0 denotes initial quantities (i.e., upon entry to the wiggler at $z=0$), p_0 and Δp_z denote the initial bulk momentum and momentum spread, respectively,

H is the Heaviside function, and the normalization constant is

$$A \equiv \left[\pi \int_0^{p_0} dp_{z0} \exp[-(p_{z0}-p_0)^2/\Delta p_z^2] \right]^{-1} . \quad (15)$$

Note that while this distribution is monoenergetic, there is an axial energy spread which is given by

$$\frac{\Delta\gamma_z}{\gamma_0} = 1 - \left[1 + 2(\gamma_0^2 - 1)\frac{\Delta p_z}{p_0} \right]^{-1/2} , \quad (16)$$

where $\gamma_0 \equiv (1+p_0^2/m_e^2c^2)^{1/2}$. The averaging operator takes the form

$$\langle (\cdots) \rangle \equiv \frac{A}{4\pi^2 w_0^2} \int_0^{2\pi} d\phi_0 \int_0^{p_0} dp_{z0} \beta_{z0} \exp[-(p_{z0}-p_0)^2/\Delta p_z^2] \int\int_{A_b} dx_0 dy_0 \sigma_\perp(x_0,y_0) \int_{-\pi}^{\pi} d\psi_0 \sigma_\parallel(\psi_0)(\cdots) , \quad (17)$$

where A_b denotes the initial cross sectional area of the beam, $\phi_0 \equiv \tan^{-1}(p_{y0}/p_{x0})$, $\beta_{z0} \equiv v_{z0}/c$, ψ_0 ($\equiv -\omega t_0$, where t_0 is the injection time) is the initial ponderomotive phase, and $\sigma_\parallel(\psi_0)$ and $\sigma_\perp(x_0,y_0)$ describe the initial beam distributions in phase and cross section.

D. Electron dynamics

These equations for the amplitude and phase of each of the Gauss-Hermite modes [(12) and (13)] are integrated simultaneously with the three-dimensional Lorentz force equations for an ensemble of electrons. As such, the procedure is capable of treating the self-consistent injection of the beam into the wiggler, emittance growth due to the inhomogeneities in the wiggler and radiation fields, betatron oscillations, and optical guiding of the radiation to list a few of the three-dimensional effects inherent in the interaction. Since this is an amplifier model, the Lorentz force equations are integrated in z and are of the form

$$v_z \frac{d}{dz}\mathbf{p} = -e(\mathbf{E}^{(s)}+\delta\mathbf{E}) - \frac{e}{c}\mathbf{v}\times(\mathbf{B}_w+\mathbf{B}^{(s)}+\delta\mathbf{B}) , \quad (18)$$

where $\mathbf{B}_w$ is the wiggler field, $\delta\mathbf{E}$ and $\delta\mathbf{B}$ are the electromagnetic fields associated with the total vector potential (9),

$$\delta\mathbf{E} = -\frac{1}{c}\frac{\partial}{\partial t}\delta\mathbf{A} \quad (19)$$

and

$$\delta\mathbf{B} = \nabla\times\delta\mathbf{A} . \quad (20)$$

In addition, $\mathbf{E}^{(s)}$ and $\mathbf{B}^{(s)}$ represent the self-electric and self-magnetic fields associated with the bulk charge and current distribution of the beam.

The technique used in the treatment of the self-electric and -magnetic fields has been described previously [21] and has been shown to give good agreement with a collective FEL experiment [27]. Under the assumption of a flat-top density profile the self-fields can be expressed as

$$\mathbf{E}^{(s)} = -\frac{m_e}{2e}\omega_b^2[(x-\langle x\rangle)\hat{\mathbf{e}}_x + (y-\langle y\rangle)\hat{\mathbf{e}}_y] \quad (21)$$

and

$$\mathbf{B}^{(s)} = -\frac{m_e}{2e}\omega_b^2\langle\beta_z\rangle[(y-\langle y\rangle)\hat{\mathbf{e}}_x - (x-\langle x\rangle)\hat{\mathbf{e}}_y] , \quad (22)$$

where $\langle x\rangle$ and $\langle y\rangle$ specify the beam centroid, the $\langle\beta_z\rangle$ is the average axial beam velocity. In order to make use of this approach, these average beam quantities must be determined at each point in the integration prior to the calculation of the self-fields. In addition, the beam initialization must include the space-charge depression in electron energy across the beam profile. This energy variation takes the form

$$\gamma(r) = \gamma_0 + \frac{\omega_b^2}{4c^2}(r^2 - R_b^2) \quad (23)$$

for an initial beam radius R_b, and results in an energy spread which may be expressed as

$$\frac{\Delta\gamma_{\text{self}}}{\gamma_0} \approx 5.88\times10^{-5}\frac{I_b}{\sqrt{\gamma_0^2-1}} , \quad (24)$$

where the beam current I_b is in A. It should be noted that this represents a coherent energy spread across the beam and is not the same as a thermal energy spread.

It should be remarked here that, in contrast to Maxwell's equations, there is no necessity to average the orbit equations. Recall that the amplifier model used is based upon the propagation of a single frequency wave, and that the interaction is resonant at the frequency where the bulk velocity of the electron beam is in synchronism with the phase velocity of the ponderomotive wave, i.e., $v_b \approx \omega/(k+k_w)$. Since the electromagnetic field in the Lorentz force equations is evaluated along the electron trajectory, the bulk phase (apart from the components which describe diffraction) varies as $\varphi = kz - \omega t$. Substitution of $z = z_0 + \omega t/(k+k_w)$ in this expression for the phase yields $\varphi \approx kz_0 - ck_w t$ under the assumption that $k \approx \omega/c \gg k_w$. As a result, the contributions due to the electromagnetic fields in the Lorentz force equations vary on the scale length of the wiggler period, and the integration step need only be small enough to resolve this spatial scale.

III. NUMERICAL ANALYSIS

The set of coupled nonlinear differential equations for the amplitudes and phases of the Gauss-Hermite modes (12) and (13) are solved numerically in conjunction with the Lorentz force equations (18) for an ensemble of electrons. In general, Eqs. (13) and (14) are second order in the amplitude and phase, but it will prove numerically

convenient in many cases to neglect the second derivatives of the amplitude and phase, and to integrate the resulting first-order equations. The error associated with this approximation is, typically, small while the numerical stability is much improved. The algorithm employed for this purpose is a fourth-order Runge-Kutta-Gill technique, and the particle averages are carried out using a Gaussian quadrature technique in each of the degrees of freedom $(x_0, y_0, \psi_0, \phi_0, p_{z0})$. For cases discussed in this paper, a choice of 1000 particles was found to be adequate when $\Delta\gamma_z = 0$, which is increased to 9600 particles otherwise. The number of Gauss-Hermite modes necessary to describe the evolution of the electromagnetic field depends upon the detailed parameters of each particular example. Diffraction over the Rayleigh length is countered by optical guiding due to the beam, and the detailed balance depends upon the Rayleigh length, the growth rate, and the evolution of the beam envelope in the wiggler. As a result, the specific number of modes used in each case is determined by an empirical procedure in which successive simulation runs are made with increasing number of modes until convergence of the saturation power and saturation length are achieved.

The initial conditions are chosen to model the injection of a solid axisymmetric and monoenergetic electron beam with a uniform cross section. As mentioned previously, there is a coherent variation in the kinetic energy across the beam which is countered by a similar variation in the potential energy due to the self-electric field. The Gauss-Hermite modes are initially assumed to be at the free-space wavelength and it is assumed that the radiation waist is located at $z = 0$ with a spot size equal to the beam radius, although this can be altered to model the injection of power in a given mode with a different spot size. The initial power levels in each mode can be arbitrarily selected to describe the injection of a specific pulse or of noise. For each case discussed in this paper, however, it is assumed that the total initial power is in the lowest-order mode, and all higher-order modes grow from zero power due to the interaction with the electron beam.

It should be remarked that no attempt is made to "match" the beam upon entry to the wiggler in the sense that the beam emittance and radius are selected in order to ensure that the beam envelope remains constant. In the opinion of the author, this is a pointless and counterproductive procedure both from an experimental and theoretical standpoint. Radiation growth in a FEL is a microscopic process in which resonant electrons interact with the radiation field, and give rise to both amplification and refractive guiding of the wave. The interaction is extremely sensitive to the axial energy spread (or emittance) of the beam, and even a small axial energy spread can result in a substantial reduction in the peak extraction efficiency. In contrast, efforts to "match" the beam are motivated by the desire to achieve a uniform beam envelope in the hope that this will yield an improved overlap between the electron beam and the radiation field or, in other words, to maximize the filling-factor and the growth rate. However, the overlap between the beam and the radiation is a macroscopic process depending upon the growth and refractive guiding determined by the microscopic interaction. Hence, it is more important to minimize the emittance in a FEL than it is to match the electron beam to achieve a uniform envelope. Variations in the beam centroid due to the wiggler motion and the beam envelope due to betatron oscillations will merely result in guiding of the signal, while an enhanced emittance which may be necessary to match the beam will certainly result in a degradation in the extracted power. The most important consideration in the design of a FEL, therefore, is to minimize the emittance.

Two cases will be examined in this paper. The first is an infrared FEL operating at wavelengths in the neighborhood of 3.5 μm, and the second is an x-ray FEL operating at wavelengths near 1.4 Å. It will be assumed in both cases that the injected signal is at a power level of 10 kW. While this may be unrealistic if actual devices in these spectral ranges are operated in SASE mode, the analysis will still serve to determine essential characteristics of the interaction such as the extraction efficiency, sensitivity to emittance, mode character, and the effects of wiggler imperfections.

For convenience, the simulation will be referred to as MEDUSA.

A. Infrared FEL

In treating the infrared FEL, it is assumed that a 30-MeV/100-A electron beam with an initial radius of 0.0525 cm propagates through the drift tube in the presence of a planar wiggler with an amplitude of 5.2 kG, a period of 1.8 cm, and an entry taper region which is 10 wiggler periods in length. The specific radius of the drift tube is not important as long as it is much greater than the beam radius. In this case, the second wiggler model [(2)–(5)] is used with a choice of $m = 2$ and $\alpha_x = 0.2$ cm, and it should be noted that the detailed results will vary somewhat with these parameters. The initial spot size is assumed to be equal to the beam radius ($w_0 = 0.0525$ cm) and that an initial power of 10 kW is injected into the TEM_{00} mode. Note that while the Gauss-Hermite modes are only approximately TEM modes in the limit in which $\lambda \ll w_0$ and R_b, it is convenient to refer to them with this notation.

The first issue to be addressed is the growth of the signal for an ideal beam in which $\Delta\gamma_z = 0$ and the mode spectrum which results therefrom. The results from MEDUSA for the choice of $\lambda = 3.505$ μm are shown in Fig. 1, illustrating the evolution of the power versus axial position for the total signal and for the TEM_{00} mode. It is clear from the figure that the total signal grows in an approximately exponential fashion until saturation is reached at a power level of approximately 8.9 MW at $z/\lambda_w \approx 199$. This represents an efficiency of approximately 0.27% and an average growth rate for all modes of $|\mathrm{Im}k|/k_w \approx 2.69 \times 10^{-3}$. It is also clear from the figure that while the TEM_{00} mode was the dominant mode upon injection of the signal, higher-order modes grow rapidly. At saturation, the TEM_{00} mode power is 1.69 MW, which accounts for only 19% of the total power.

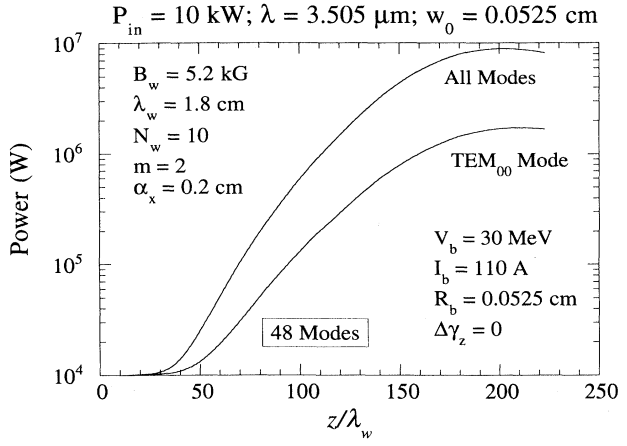

FIG. 1. Evolution of the power versus axial distance for an ideal beam.

The growth of higher-order modes depends upon specific details of the beam radius, wiggler amplitude (and, hence, the beam displacement for the midplane), and the radiation spot size and Rayleigh length. It is found that for the fundamental resonance represented by this case that the only TEM_{ln} modes which grow are those for which both l and n are even, and the ones which grow most rapidly are those where either l or n are zero. While the TEM_{00} mode represents less than half the total power at saturation, it is still the dominant mode. The TEM_{02} and TEM_{20} modes are the next highest at power levels approximately 45% that of the TEM_{00} mode. The power decreases rapidly for higher-order modes; however, some 48 modes must be retained in order for the mode superposition to converge to within better than 1% accuracy. This is illustrated in Fig. 2, in which the relative mode amplitudes (normalized to the power in the TEM_{00} mode) are shown at saturation. As shown in the figure, the bulk of the power is contained within five modes (the TEM_{00}, TEM_{02}, TEM_{20}, and TEM_{04}, and TEM_{40}), but substantial amounts of power are found in the tail of the superposition.

The even modes are seen to interact preferentially at the fundamental resonance; however, this does not mean that odd modes do not interact. It is expected that the even modes will also be preferentially amplified by interactions at odd harmonics, the odd modes will yield amplification at even harmonics by a periodic position interaction. This has been demonstrated at microwave frequencies in both theory and experiment at the Naval Research Laboratory [28], and in theory at infrared wavelengths at Los Alamos National Laboratory [29]. Harmonic interactions, however, will be discussed in a future paper.

The broad mode spectrum is not an artifact of the initial "top-hat" radial density profile. A parabolic density profile has also been used and, for a fixed total current, yielded a result which differed from the top-hat distribution by only a few percent. The principal reason for this is that the radial distribution describes only the initial state of the beam. The subsequent beam evolution is governed by the three-dimensional wiggler, radiation, and self-fields and the radial profile of the beam is quickly distorted from the initial state.

The importance of self-fields on the interaction can be illustrated by examining the resonant spectrum. The efficiency is plotted as a function of wavelength in Fig. 3 for an ideal beam subject to both the inclusion and neglect of the self-fields. The resonant interaction is seen to extend from a wavelength of approximately 3.47 μm through 3.52 μm with the peak efficiency found at the longer wavelengths. The effect of the self-fields for this case is to uniformly reduce the efficiency. At 3.5 μm, the efficiency drops from 0.30% without the self-fields to 0.27% with the self-fields which represents a 10% drop in efficiency. A similar decrease due to the self-fields is also found in the average growth rate as shown in Fig. 4. Here, the average growth rate at 3.505 μm decreases from $|\mathrm{Im}k|/k_w \approx 2.82\times10^{-3}$ without the self-fields to 2.69×10^{-3} with the inclusion of the self-fields. Note that this 10% drop in the efficiency is associated with a

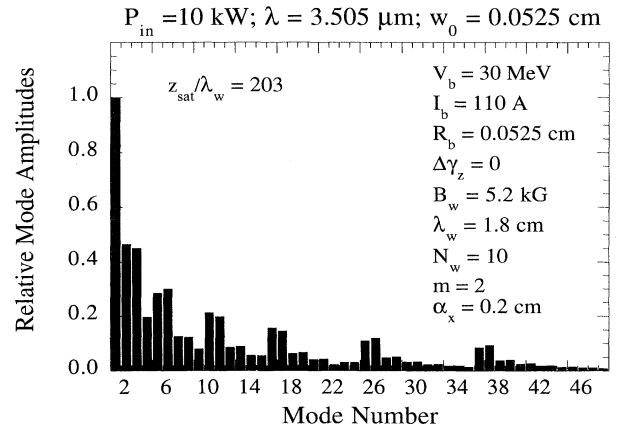

FIG. 2. Relative mode amplitudes at saturation as normalized to the power in the TEM_{00} mode.

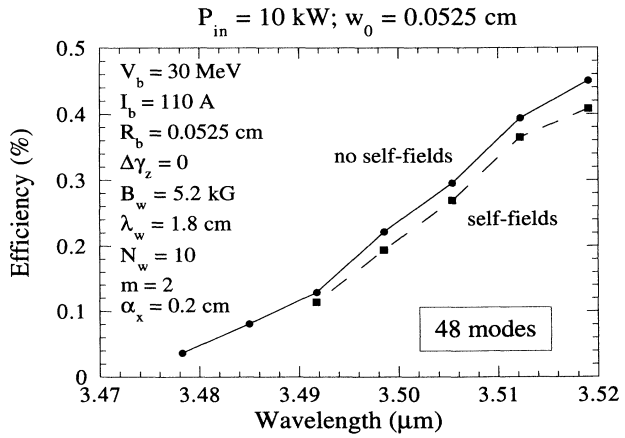

FIG. 3. Plot of the efficiency versus wavelength both with and without the self-fields.

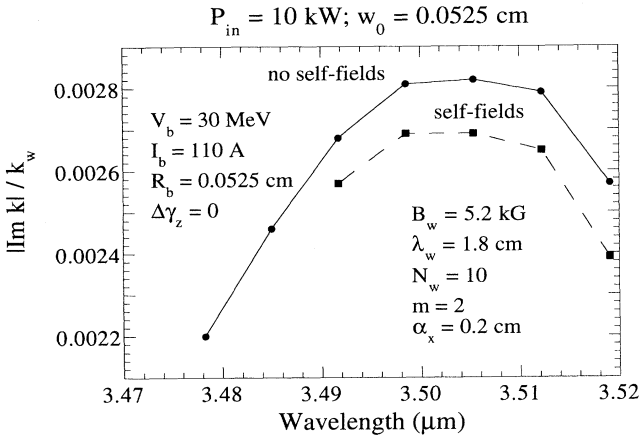

FIG. 4. Plot of the average growth rate versus wavelength with and without the self-fields.

coherent energy drop across the beam of only $\Delta\gamma_{\rm self}/\gamma_0 \approx 0.01\%$. It should also be noted that one-dimensional phase trapping estimates of the efficiency [17] yield a value of 0.42% for the maximum efficiency, which is close to that shown in the figure.

The effect of the axial energy spread on the interaction is severe. In view of the FEL resonance condition, the transition to the thermal regime occurs for $\Delta v_z/v_0 \approx |{\rm Im}k|/[{\rm Re}k + k_w] \approx 5.24\times10^{-7}$ since $|{\rm Im}k|/k_w \approx 0.002\,69$ at a wavelength of 3.505 μm. This corresponds to an axial energy spread (16) of $\Delta\gamma_z/\gamma_0 \approx 0.19\%$. The variation in the efficiency and average growth rate with increases in the axial energy spread ($\Delta\gamma_z/\gamma_0$) is shown in Fig. 5 at a wavelength of 3.505 μm and subject to the inclusion of the self-fields over the range of axial energy spreads up to the thermal transition. It is clear from the figure that the interaction strength decreases rapidly with increases in the axial energy spread. The efficiency decreases by more than half as the energy spread increases to 0.2%, and the average growth rate also drops a significant amount from 2.69×10^{-3} to 1.86×10^{-3}. It is clear, therefore, that an experiment in this regime will require the axial energy spread to be held to less than 0.1% to realize optimal performance.

The effect of wiggler imperfections has been studied by this non-orbit-averaged approach for long-wavelength interactions in which the transverse mode pattern of the radiation is governed by the waveguide [23,24]. In such cases, the effect of wiggler imperfections was found to be small. Typically, root mean square (rms) wiggler imperfection levels of as much as a few percent were found to have negligible impact on the extraction efficiency and growth rate in a long-wavelength FEL. However, it has been suggested that this might not be the case for short-wavelength FELs. The speculation is that in the short-wavelength regime wiggler imperfections might cause the electron beam to walk off from the radiation spot thus resulting in a degradation in the efficiency and growth rate.

In order to address this speculation, we now consider the effect of the random contribution to the wiggler amplitude defined in Eqs. (6) and (8) and generate a sequence of random periodic fluctuations in the wiggler amplitude $\{\Delta B_n\}$ with a period of $\lambda_w/2$ (i.e., $N_p=2$ in the notation described in Sec. II). The effect of these wiggler imperfection distributions is studied statistically for ensembles of random sequences at fixed rms values. Typically, it is found that, at a given rms level, the ensemble averages require consideration of 35 different random sequences for the average efficiency to converge to within 1%. In order to isolate the effect of the wiggler imperfections, all such simulations are performed under the assumption of an ideal beam (i.e., $\Delta\gamma_l=0$).

MEDUSA indicates that, as in the case of the long-wavelength FELs studied previously [23,24], the effects of wiggler imperfections are also small for this infrared wavelength example. The variation in the ensemble-averaged efficiency with increases in $(\Delta B_w/B_w)_{rms}$ is shown in Fig. 6 for parameters consistent with the case shown in Fig. 1. The error bars in the figure denote the standard deviations. It is clear from the figure that the average efficiency is remarkably insensitive to the wiggler imperfections even for rms fluctuation levels as high as

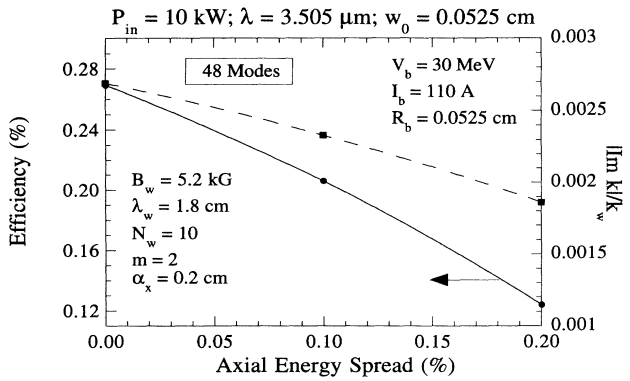

FIG. 5. Variation in the efficiency and average growth rate with axial energy spread.

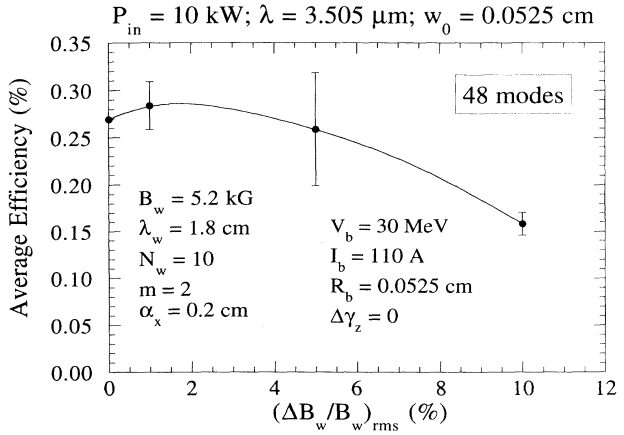

FIG. 6. Variation in the ensemble-averaged efficiency for $N_p=2$.

10%. Over this range of fluctuations, the efficiency drops by slightly less than half from 0.27% to 0.14%. More significantly, the ensemble-averaged efficiency actually increases slightly as $(\Delta B_w/B_w)_{rms}$ increases up to 2%, and drops only to 0.26% for $(\Delta B_w/B_w)_{rms}=5\%$. The reason for the small increase in the efficiency at low values of $(\Delta B_w/B_w)_{rms}$ is that the only constraint placed upon the random sequence is that of the rms fluctuation level. The average value of the wiggler fluctuation $\langle B_w \rangle$ is not constrained. Hence, what has happened is that the average value of the wiggler amplitude has increased slightly over the 5.2 kG of the uniform B_w, and this has resulted in a slight increase in the efficiency. However, this does not alter the conclusion that the interaction is relatively insensitive to imperfections in the wiggler field.

In order to explain why the effect is so small, we turn to a detailed consideration of the orbit dynamics due to the wiggler imperfections. Figure 7 shows the motion of the beam center $\langle x \rangle$ versus axial position for an ideal wiggler [i.e., $(\Delta B_w/B_w)_{rms}=0$] during the interaction shown in Fig. 1. The figure shows the spinning up of the beam in the entry taper region and the bulk wiggler-induced oscillation. The figure also shows that the beam motion is not regular but is substantially perturbed. In order to explain this, note that the beam centroid describes an average over the entire beam cross section. Electrons injected near the axis of symmetry execute an extremely regular trajectory showing largely the effects of the bulk wiggler oscillation. However, the off-axis electrons undergo substantial betatron motion under the action of both the wiggler and the radiation field. Note also that the initial beam radius $R_b \approx 0.03\lambda_w$ is substantially larger than the magnitude of the perturbations of the beam centroid; hence, these perturbations are relatively small in comparison with the scalloping of the beam envelope.

The motion of the beam center shown for the ideal wiggler is now compared with that found for the case of $(\Delta B_w/B_w)_{rms}=5\%$. The specific random sequence examined is one which gave an efficiency close to the ensemble average, and is shown in Fig. 8. A comparison of the amplification of the radiation for the ideal wiggler and for

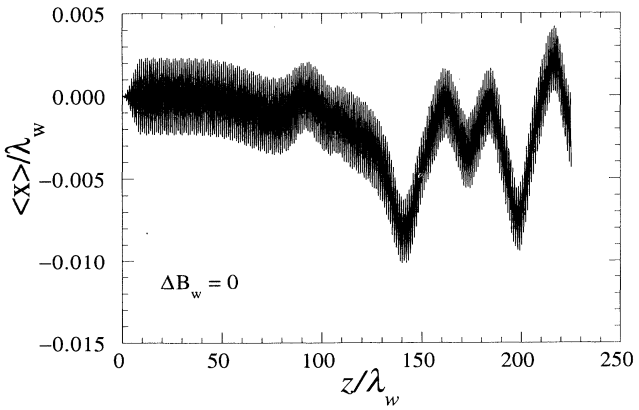

FIG. 7. Motion of the beam center versus axial position in an ideal wiggler.

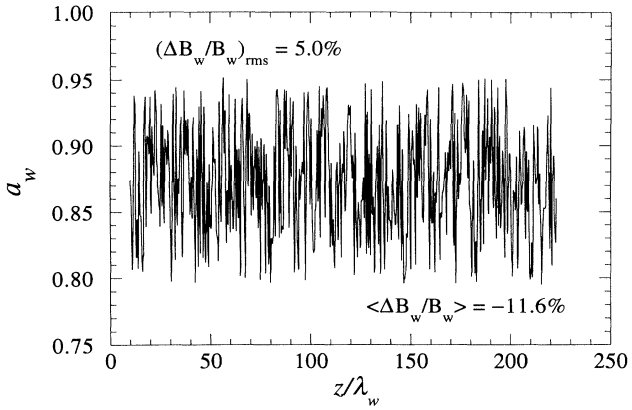

FIG. 8. Plot of the wiggler parameter for a specific random sequence.

this choice of wiggler imperfections is shown in Fig. 9. It is evident that the total extracted power drops from 8.9 MW for the ideal wiggler to approximately 8.7 MW for this choice of wiggler imperfections. The motion of the beam center in the wiggler-plane corresponding to the interaction in this particular choice of wiggler imperfections is shown in Fig. 10. It is clear from the figure that while the specific motion of the beam center has changed from that shown in Fig. 7 for an ideal wiggler, the qualitative character of the motion has not. The electron beam is kicked off-axis many times during the course of the interaction as in the case of the ideal wiggler. In this case, these perturbations are due both to the large amplitude radiation field and the wiggler imperfections. Indeed, the combined effects of the large amplitude radiation field and the wiggler imperfections in this case has led to a much smaller maximum displacement from the symmetry plane than was found in Fig. 7 for the ideal wiggler. However, there is still no coherent walk off of the beam, and while the beam may be displaced in one direction from the symmetry plane at one point in the in-

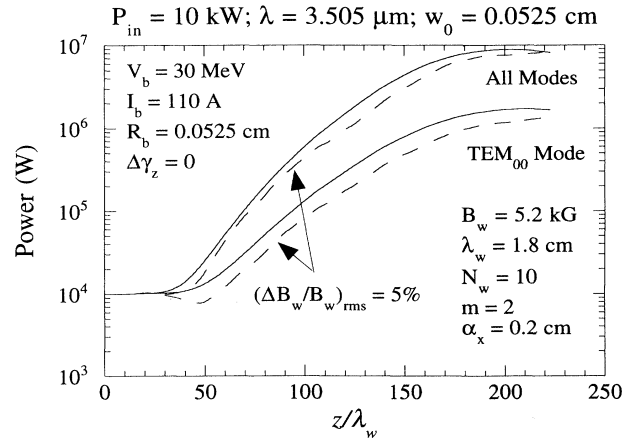

FIG. 9. Evolution of the power for an ideal wiggler (solid line) and for the random wiggler variations (dashed line) shown in Fig. 8.

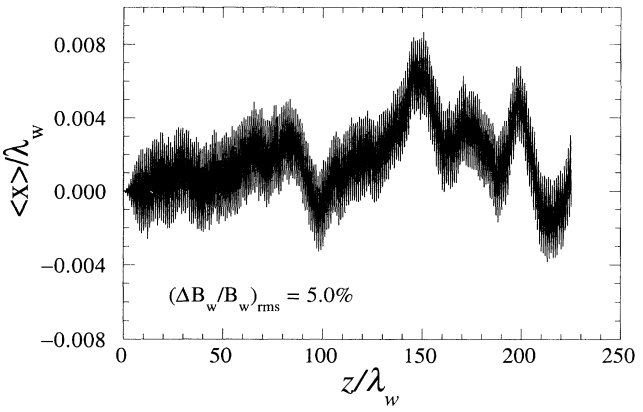

FIG. 10. Motion of the beam center versus axial position subject to wiggler imperfections.

teraction, it is displaced in the opposite direction at another point. The net result is that the beam center has returned to a point near the symmetry plane at the end of the interaction region.

The conclusions to be drawn from these results are twofold. In the first place, it does not appear that there is any serious walk off of the beam. The beam displacement from the symmetry plane can be relatively large even in the absence of wiggler imperfections when the radiation amplitude becomes large, but the effect of wiggler imperfections does not magnify this effect and can even counter it. Thus, MEDUSA does not predict any cumulative walkoff of the beam due to the wiggler imperfections. In the second place, the speculation that wiggler imperfections might result in a severe degradation in the gain and efficiency are exaggerated. The radiation is guided by the interaction. Displacements of the beam from the symmetry plane can result in the presence of a large component of higher-order modes which might negatively impact the ultimate use of the FEL; however, as attested by the fact that the maximum efficiency found from one-dimensional phase trapping arguments is close to that found by MEDUSA, the ultimate extracted power is not seriously affected. In general, therefore, the effect of wiggler imperfections is not severe, and is much less important a constraint on FEL design than the emittance of the electron beam.

B. X-ray FEL

The x-ray FEL parameters under study here correspond to the proposed LCLS at SLAC. Due to the lack of sources to drive a MOPA in this spectral band, the device would operate in the SASE mode using the SLAC linac at an energy of 15 GeV. The beam pulses would be compressed in the axial direction to achieve a peak current of 5 kA, and would have a radial extent of only 16 μm. The proposed wiggler would achieve a 16-kG amplitude at a period of 2.7 cm, and it is assumed for this study that the entry taper region is 10 wiggler periods in length. This implies a resonant wavelength in the neighborhood of 1.4 Å. As in the infrared example discussed previously, it shall also be assumed that the initial power is 10 kW in the TEM_{00} mode, and that the initial spot size matches the beam radius at 16 μm. The parabolic pole face wiggler (1) is used to study the interaction for an ideal wiggler, and the second wiggler (2) is to examine the effect of wiggler imperfections.

The issue of quantum mechanical effects should be discussed for this configuration if only for the purpose of dismissing them. Quantum mechanical effects can be neglected if the spreading of the electron wave packet over the length of the wiggler is less than the radiation wavelength. This can be formulated as [17,30]

$$\Delta z = \frac{\lambda_c L}{\gamma_0 \gamma_w} \ll \lambda \ , \tag{25}$$

where Δz denotes the spreading of the electron wave packet, $\lambda_c \equiv h/m_e c$ is the Compton wavelength, and L is the length of the wiggler. For the parameters of interest to the LCLS, the spreading of the wave packet over a wiggler length of 30 m is $\Delta z \approx 9.2 \times 10^{-4}$ Å, which is approximately three orders of magnitude less than the 1.4-Å wavelength. At this length of wiggler, therefore, quantum mechanical effects can be neglected from the treatment. However, this is the closest that any operational or proposed FEL has approached to the regime where quantum mechanical effects are important, and if a wiggler of 100 m or more in length were required, then quantum mechanical effects might become important. Finally, another requirement for the neglect of quantum mechanical effects is that the electron recoil on emission of a photon is small. This can be formulated by the requirement that the frequency downshift in the emitted photon due to the electron recoil is less than the gain linewidth, and results in a criterion identical to (25).

First consider the interaction for the TEM_{00} mode alone. The spectrum is shown in Fig. 11 in which we plot the extraction efficiency versus wavelength for an ideal beam and both with and without the self-fields. As shown in the figure, the efficiency subject to the inclusion of the self-fields peaks at 0.97% at a wavelength of ap-

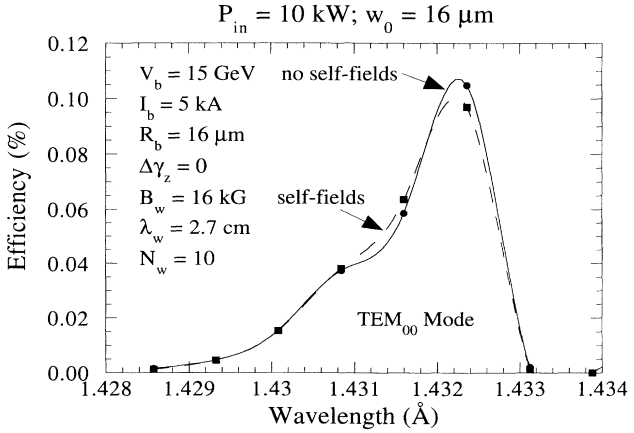

FIG. 11. Efficiency versus wavelength for single mode propagation.

proximately 1.4323 Å. The effect of the self-fields is small, but results in a decrease in the peak efficiency of approximately 7.5%. In contrast to the results for the infrared example, the effect of self-fields can result in slight enhancements in the efficiency in narrow parts of the spectrum.

In this example, it is found that adequate convergence of the mode superposition is achieved using 38 modes. A plot of the power as a function of axial position is shown in Fig. 12 for an ideal beam at a wavelength of 1.4323 Å. The interaction saturates at a power of approximately 98 GW for an efficiency of 0.13% over an interaction length of 30 m. This contrasts with a saturated power level of about 73 GW over a saturation length of 52 m, which is found using the TEM_{00} mode alone. As a consequence, as in the infrared example, while the TEM_{00} mode is dominant, it constitutes only about 27% of the total power at saturation. The relative mode amplitudes at saturation are shown in Fig. 13 and are normalized to the power in the TEM_{00} mode. It is clear that, as in the infrared example, the dominant modes are the TEM_{00}, TEM_{02}, TEM_{20}, TEM_{04}, and TEM_{40}, but substantial amounts of power are contained in the higher-order modes.

As might be expected, the interaction for the x-ray FEL is more sensitive to the axial energy spread than the infrared case. The average growth rate associated with the interaction in Fig. 12 is $|\mathrm{Im}k|/k_w \approx 1.15\times10^{-3}$, which implies that the transition to the thermal regime is found for $\Delta\gamma_z/\gamma_0 \approx 0.05\%$. A plot of the variation in the extraction efficiency and the saturation length at a wavelength of 1.4323 Å spanning the thermal transition regime is shown in Fig. 14. As shown in the figure, the extraction efficiency drops by more than half as the axial energy spread increases to 0.1%, and by 39% at the thermal transition. The growth rate also decreases, and the saturation length increases from about 30 m for an ideal beam to 39 m at the high end of this range. As such, it is necessary to keep the beam emittance as small as possible to remain far below the thermal transition for optimal performance, and the achievement of near-peak

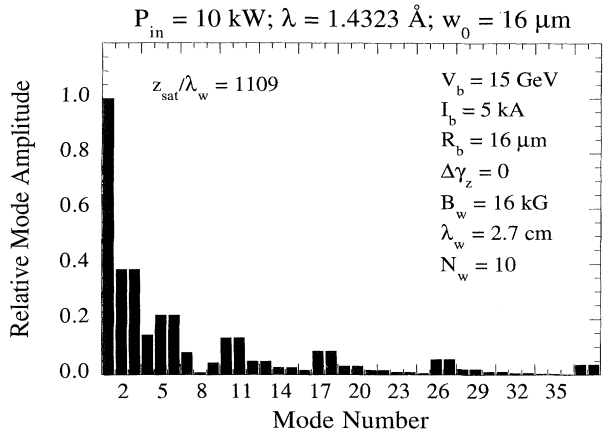

FIG. 13. Relative mode amplitudes at saturation as normalized to the power in the TEM_{00} mode.

efficiencies requires that $\Delta\gamma_z/\gamma_0 \leq 0.015\%$.

The effect of wiggler imperfections on the LCLS design is studied using the second wiggler model (2). The identical beam ($V_b=15$ GeV, $I_b=5$ kA, $R_b=16$ μm), wiggler ($B_w=16$ kG, $\lambda_w=2.7$ cm, $N_w=10$), and radiation ($P_{in}=10$ kW, $\lambda=1.4323$ Å, $w_0=16$ μm, 38 modes) parameters are used for this purpose as were used previously with the parabolic pole face wiggler model, except that we also assume that $m=2$ and $\alpha_x=0.1$ cm for the second wiggler model. The evolution of the power with axial position for an ideal wiggler is shown in Fig. 15 for purposes of comparison. As is evident in the figure, the power saturates at approximately 97 GW over a length of 30 m for an overall extraction efficiency of about 0.13%. This is very close to the results found for the parabolic pole face wiggler (97 MW over a saturation length of 30 m).

The motion of the beam center in the x direction (the direction of the principal wiggler-induced transverse velocity) is shown in Fig. 16 for the ideal wiggler case corresponding to that shown in Fig. 15. In contrast to the re-

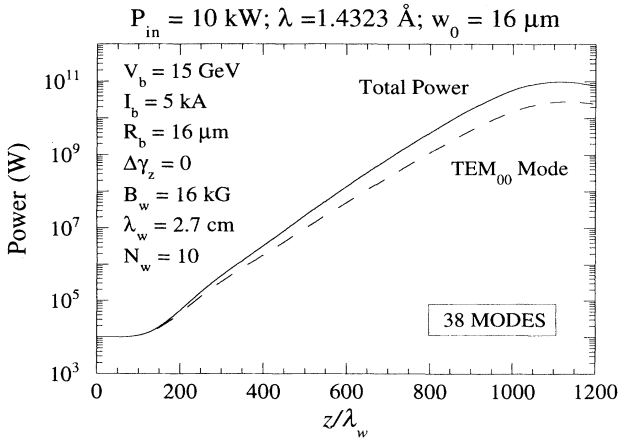

FIG. 12. Evolution of the power versus axial position.

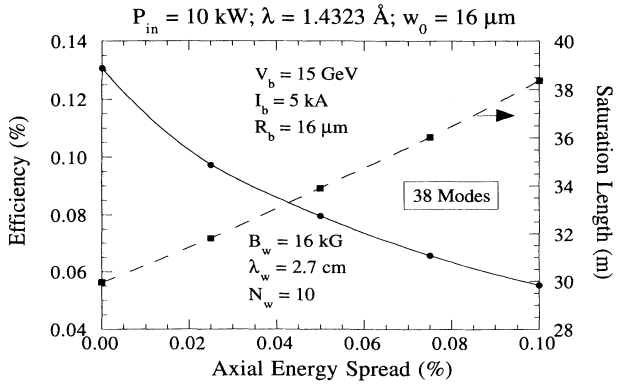

FIG. 14. Variation in the efficiency and saturation length versus axial energy spread.

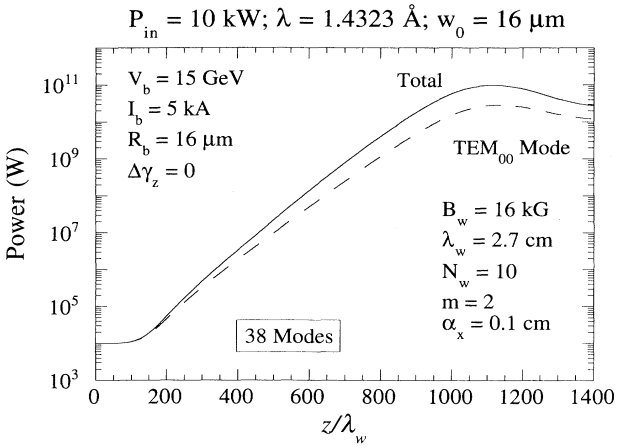

FIG. 15. Evolution of the power versus axial position for the LCLS parameters in an ideal wiggler using the second wiggler model. The solid (dashed) line denotes the total (TEM_{00} mode) power.

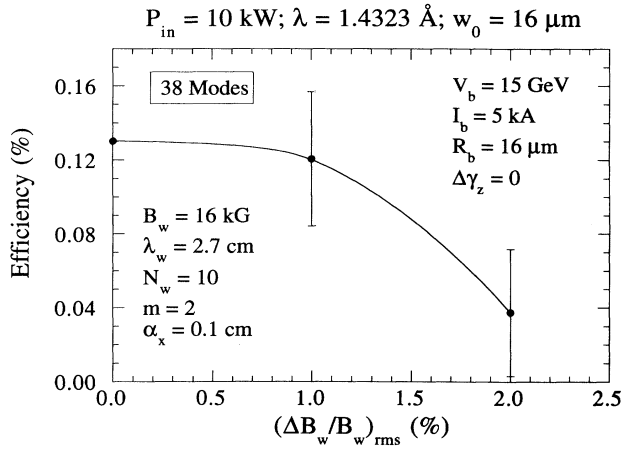

FIG. 17. Variation in the ensemble-averaged efficiency for $N_p=2$.

sults found for the 30-MeV beam and 3.5-μm radiation (see Fig. 7), the wiggler motion for the LCLS parameters in the absence of wiggler imperfections is extremely uniform. There is very little wandering of the beam center due to the high-amplitude radiation field, and the beam exhibits the bulk wiggler motion as well as the expected betatron oscillations. This is due to the increased "stiffness" of the 15-GeV beam, and accounts for the fewer number of modes needed relative to the infrared example.

The effect of wiggler imperfections for LCLS parameters is greater than for the infrared example, but still not severe. In studying the effect of wiggler imperfections, it is assumed, as in the preceding example, that the random wiggler amplitude variations occur every half wiggler period (i.e., $N_p=2$). The variation in the efficiency with increasing values of $(\Delta B_w/B_w)_{rms}$ is shown in Fig. 17. As in the preceding example, the dots in the figure represent the ensemble average over 35 randomly chosen

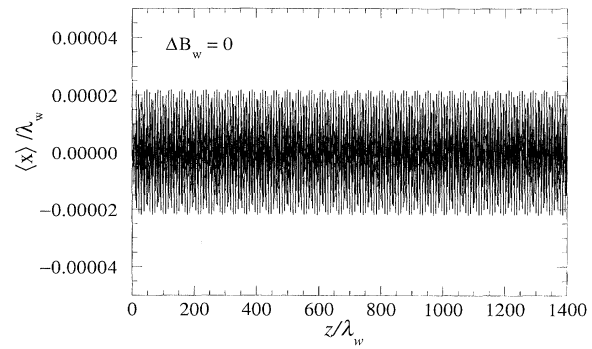

FIG. 16. Motion of the beam center versus axial position in an ideal wiggler for the LCLS parameters.

amplitude fluctuation distributions, and the "error bars" denote the standard deviations. It is clear from the figure that the efficiency remains relatively unaffected by the wiggler imperfections for $(\Delta B_w/B_w)_{rms}\leq 1\%$, and decreases rapidly thereafter. The efficiency for the ideal wiggler in this case is 0.13%, which decreases to 0.12% for $(\Delta B_w/B_w)_{rms}=1\%$. This represents a negligible degradation in the interaction efficiency, and it is reasonable to conclude that the LCLS will operate up to nearly optimum efficiencies as long as the rms wiggler imperfections are kept to within this limit.

However, the LCLS parameters do exhibit a greater sensitivity to wiggler imperfections than was found for the preceding infrared wavelength FEL example. This is expected due to the narrower radius of the 15-GeV beam. In general, the smaller the beam radius, the more difficult it is for the interaction to guide the radiation. However, this is offset in the present case by the greater stiffness of the 15-GeV beam, which requires a relatively large level of wiggler imperfections to cause any appreciable beam deflection.

In order to illustrate the effect of the wiggler imperfections, we turn to a more detailed consideration of the orbit dynamics for a specific choice of wiggler imperfections. For this purpose, we compare the motion of the beam center for an ideal wiggler shown in Fig. 16 with the corresponding motion for $(\Delta B_w/B_w)_{rms}=1\%$ and the specific random sequence which resulted in an efficiency of 0.12% (i.e., which was chosen to the ensemble average). The variation in the wiggler parameter a_w for this case is shown in Fig. 18, and the motion of the beam center for this choice is shown in Fig. 19. It is clear from Fig. 19 that the variation in the beam center is relatively slow for this case, and that there is no coherent walkoff of the beam.

In this example, the beam is able to guide the radiation, and although the maximum displacement of the beam center relative to that found for an ideal wiggler is approximately 50% that of the maximum bulk wiggler-

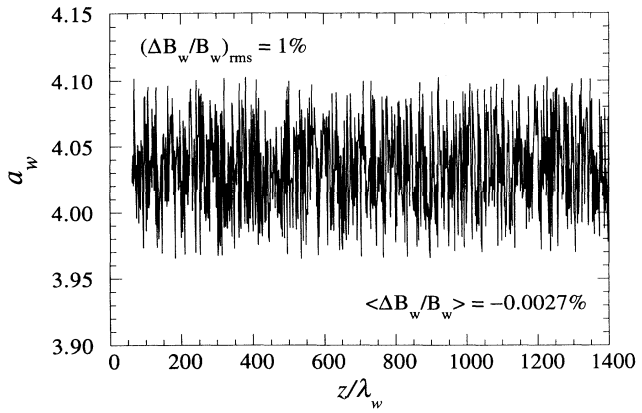

FIG. 18. Plot of the wiggler parameter for a specific random sequence.

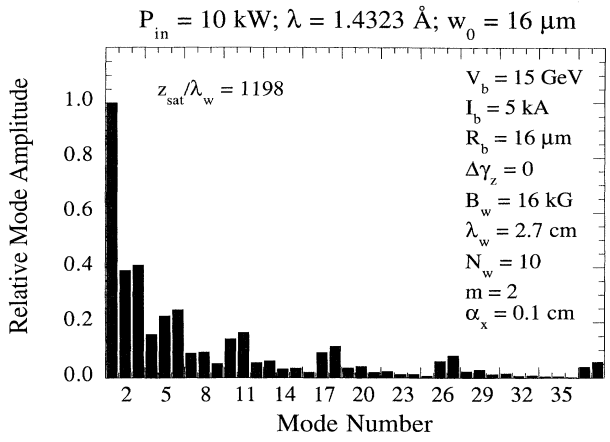

FIG. 20. Relative mode amplitudes at saturation normalized to the TEM_{00} mode subject to the wiggler imperfections shown in Fig. 18.

induced oscillation (at $z/\lambda_w \approx 150$), there is little degradation in the interaction efficiency. In order to illustrate the effect of the optical guiding, consider the relative mode amplitudes at saturation. The relative mode spectrum for this case as shown in Fig. 20. A comparison of the mode amplitudes shown in Fig. 20 with those shown in Fig. 13 for the ideal wiggler indicates a somewhat larger amount of power in the higher-order modes. This reflects the fact that the beam sweeps out a greater cross sectional area for this case than for the ideal wiggler, which implies that the radiation has been guided during the course of the interaction.

The overall conclusion from this study of the effects of beam energy spread and wiggler imperfections for the LCLS parameters is that optimal performance requires that the axial energy spread be kept small enough that $\Delta\gamma_z/\gamma_0 \leq 0.01\%$ and that the rms wiggler tolerances be kept to $(\Delta B_w/B_w)_{rms} \leq 1\%$. In general, the conclusion formed on the basis of both the infrared and x-ray examples studied here is that the electron beam quality imposes a more severe constraint on the interaction than does the wiggler quality.

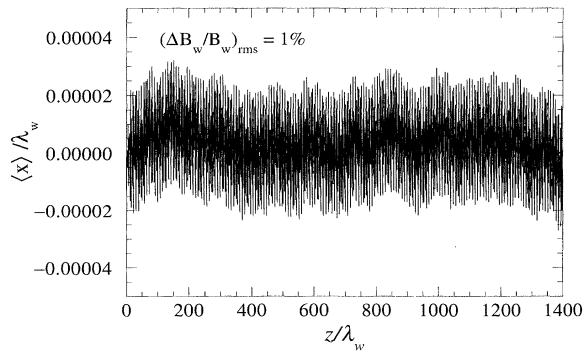

FIG. 19. Motion of the beam center versus axial position subject to wiggler imperfections.

IV. SUMMARY AND DISCUSSION

In this paper, a three-dimensional nonlinear formulation of the interaction in short-wavelength FELs is presented and used to evaluate the performance of several tentative experimental designs. For this purpose, the analysis is based upon a representation of the electromagnetic field as a superposition of the Gauss-Hermite optical modes which is appropriate for the planar wiggler configuration which is also assumed. Note that the Gauss-Laguerre modes would form the appropriate basis for a helical wiggler configuration. A set of coupled nonlinear differential equations is derived for the evolution of the amplitude and phase of each mode which is then integrated in conjunction with the three-dimensional Lorentz force equations for an ensemble of electrons.

It is important to emphasize that no wiggler average is performed on the Lorentz force equations, and that the orbits are integrated in the complete field structure including the magnetostatic wiggler, the electromagnetic fields, and the self-electric and self-magnetic fields formed by the bulk charge and current densities of the beam. As a result, it is necessary only to specify the characteristics of the beam upon entry to the wiggler and the emittance growth and evolution of the electron beam due to such effects as (1) the injection of the beam into the wiggler, (2) transverse inhomogeneities of the wiggler field (including betatron oscillations), (3) the interaction with the electromagnetic field, (4) the self-electric and self-magnetic fields of the beam, and (5) wiggler imperfections are implicitly included in the treatment.

It should be remarked in regard to the modeling of wiggler imperfections that all that is necessary is to specify the variation in the wiggler field amplitude as a function of axial position, and the simulation will self-consistently describe the response of the electron beam. Because of this, it is possible to model the imperfections of any specific wiggler magnet, although this was not attempted in the present work.

No attempt has been made to match the beam into the wiggler in the sense that the beam emittance and radius are selected to ensure that the beam envelope remains constant. In the opinion of the author, this is a pointless and counterproductive procedure both from an experimental and theoretical standpoint. Radiation growth is a microscopic process in which resonant electrons interact with the radiation field, and give rise to both amplification and refractive guiding of the wave. The interaction is extremely sensitive to the emittance of the beam, and even a small axial energy spread can result in a substantial reduction in the peak extraction efficiency. Efforts to match the beam are motivated by the desire to achieve a uniform beam envelope in the hope that this will yield an improved overlap between the electron beam and the radiation field or, in other words, to maximize the filling factor and the growth rate. However, the overlap between the beam and the radiation is a macroscopic process depending upon the growth and refractive guiding determined by the microscopic interaction. Hence, it is more important to minimize the emittance in a FEL than it is to match the electron beam to achieve a uniform envelope. Variations in the beam centroid due to the wiggler motion and the beam envelope due to betatron oscillations will merely result in guiding of the signal, while an enhanced emittance which may be necessary to match the beam will certainly result in a degradation in the extracted power. The most important consideration in the design of a FEL, therefore, is to minimize the emittance.

In general, the conclusion formed on the basis of both the infrared and x-ray examples studied here is that the electron beam quality must be kept small enough that the interaction is far from the transition to the regime where thermal effects become important. However, the interaction was found to be relatively insensitive to wiggler imperfections. In this regard, it should be emphasized that no coherent walkoff of the beam has been detected in simulation, and that the optical guiding of the radiation field is able to counter much of the jitter of the beam. Hence, it is found that electron beam quality imposes a much more severe constraint on the interaction than does the wiggler quality.

ACKNOWLEDGMENTS

The author would like to acknowledge ongoing discussions with Dr. S. Krinsky and Dr. L. H. Yu at Brookhaven National Laboratory and Dr. R. Tatchyn and Dr. Whittum at the Stanford Linear Accelerator Center. This work was supported by the Office of Naval Research. The computational work was supported in part by a grant of HPC time from the DoD HPC Shared Resource Center CEWES on a Cray C90 and a Y-MP, and in part by a grant of HPC time from the DoD HPC Center NAVO on a Cray C90.

[1] R. M. Phillips, IRE Trans. Electron Dev. **ED-7**, 231 (1960).

[2] L. R. Elias, W. M. Fairbank, J. M. J. Madey, G. J. Ramian, H. A. Schwettman, and T. I. Smith, Phys. Rev. Lett. **36**, 717 (1976).

[3] K. L. Felch, L. Vallier, J. M. Buzzi, P. Drossart, H. Boehmer, H. J. Doucet, B. Etlicher, and C. Rouillé, IEEE J. Quantum Electron. **QE-17**, 1354 (1981).

[4] R. K. Parker, R. H. Jackson, S. H. Gold, H. P. Freund, V. L. Granatstein, P. C. Efthimion, M. Herndon, and A. K. Kinkead, Phys. Rev. Lett. **48**, 238 (1982).

[5] M. Billardon, P. Ellaume, J. M. Ortega, C. Bazin, M. Bergher, M. Velghe, D. A. G. Deacon, and Y. Petroff, Phys. Rev. Lett. **51**, 1652 (1983).

[6] R. W. Warren, B. E. Newnam, J. G. Winston, W. E. Stein, L. M. Young, and C. A. Brau, IEEE J. Quantum Electron. **QE-19**, 391 (1983).

[7] J. Fajans, G. Bekefi, Y. Z. Yin, and B. Lax, Phys. Rev. Lett. **53**, 246 (1984).

[8] J. M. Slater, T. Churchill, D. C. Quimby, K. E. Robinson, D. Shemwell, A. Valla, A. A. Vetter, J. Adamski, W. Gallagher, R. Kennedy, B. Robinson, D. Shoffstall, E. Tyson, and A. Yeremian, Nucl. Instrum. Methods Phys. Res. Sect. A **250**, 228 (1986).

[9] J. C. Goldstein, B. E. Newnam, R. W. Warren, and R. L. Sheffield, Nucl. Instrum. Methods Phys. Res. Sect. A **250**, 4 (1986).

[10] J. Masud, T. C. Marshall, S. P. Schlesinger, and F. G. Yee, Phys. Rev. Lett. **56**, 1567 (1986).

[11] T. J. Orzechowski, B. R. Anderson, J. C. Clark, W. M. Fawley, A. C. Paul, D. Prosnitz, E. T. Scharlemann, S. M. Yarema, D. B. Hopkins, A. M. Sessler, and J. Wurtele, Phys. Rev. Lett. **57**, 2172 (1986).

[12] L. R. Elias, IEEE J. Quantum Electron. **QE-23**, 1470 (1987).

[13] T. I. Smith, H. A. Schwettman, R. Rohatgi, Y. Lapierre, and J. Edighoffer, Nucl. Instrum. Methods Phys. Res. Sect. A **259**, 1 (1987).

[14] V. N. Litvinenko and V. N. Vinokurov, Nucl. Instrum. Methods Phys. Res. Sect. A **304**, 66 (1991).

[15] J. M. Ortega, M. Bergher, R. Chaput, A. Dael, M. Velghe, Y. Petroff, J. C. Bourdon, R. Belbeoch, P. Brunet, Y. Dabin, B. Mouton, J. P. Perrine, E. Plouvier, R. Pointal, M. Renard, M. Roch, J. Rodier, P. Roudier, Y. Thiery, P. Bourgeous, P. Carlos, C. Hezard, J. Fagot, J. L. Fallou, P. Garganne, J. C. Malglaive, and D. T. Tran, Nucl. Instrum. Methods Phys. Res. Sect. A **285**, 97 (1989).

[16] D. A. Jaroszynzki, R. J. Bakker, A. F. G. van der Meer, M. Oepts, and P. W. van Amersfoort, Phys. Rev. Lett. **71**, 3798 (1993).

[17] H. P. Freund and T. M. Antonsen, Jr., *Principles of Free-electron Lasers* (Chapman & Hall, London, 1992).

[18] H. P. Freund and T. M. Antonsen, Jr., *Principles of Free-electron Lasers* (Ref. [17]), Chap. 5.

[19] A. K. Ganguly and H. P. Freund, Phys. Rev. A **32**, 2275 (1985).

[20] H. P. Freund, Phys. Rev. A **37**, 3371 (1988).

[21] H. P. Freund, R. H. Jackson, and D. E. Pershing, Phys.

Fluids B **5**, 2318 (1993).

[22] H. Winick, K. Bane, R. Boyce, G. Loew, H. D. Nuhn, J. Paterson, P. Pianetta, T. Raubenheimer, J. Seeman, R. Tatchyn, V. Vylet, C. Pellegrini, J. Rosenzweig, G. Travish, D. Prosnitz, E. T. Scharlemann, K. Halbach, K. J. Kim, and M. Xie, in *Proceedings of the 1993 IEEE Particle Accelerator Conference* (IEEE, Piscataway, NJ, 1993), p. 1445.

[23] H. P. Freund and R. H. Jackson, Phys. Rev. A **45**, 7488 (1992).

[24] H. P. Freund and R. H. Jackson, Nucl. Instrum. Methods Phys. Res. Sect. A **331**, 461 (1993).

[25] H. Bluem, R. H. Jackson, H. P. Freund, D. E. Pershing, and V. L. Granatstein, Phys. Rev. Lett. **67**, 824 (1991).

[26] D. Marcuse, *Light Transmission Optics* (Van Nostrand, New York, 1982), Chap. 6.

[27] D. E. Pershing, R. D. Seeley, R. H. Jackson, and H. P. Freund, Nucl. Instrum. Methods Phys. Res. Sect. A **358**, 104 (1995).

[28] H. Bluem, R. H. Jackson, H. P. Freund, D. E. Pershing, and V. L. Granatstein, Phys. Rev. Lett. **67**, 824 (1991).

[29] M. J. Schmitt and B. D. McVey, Nucl. Instrum. Methods Phys. Res. Sect. A **304**, 571 (1991).

[30] C. A. Brau, *Free-Electron Lasers* (Academic, Boston, 1990).